ADVANCED MATERIALS INTERFACES
www.advmatinterfaces.de

Wettability Engineering for Studying Ion Transport in 2D Layered Materials

*Matthias Kühne, Dong Zhao, Ute Zschieschang, Regina Buck, Michaela Müller, Hagen Klauk, and Jurgen H. Smet**

Layered materials are widely used for their capacity to incorporate and store foreign ionic species. It has become possible to exploit this process at the level of single crystals consisting of individual atomic layers: 2D materials and their van der Waals heterostructures. Due to the small size of available high-quality specimen, however, it remains challenging to probe ion transport and storage in these systems. To promote future advances in this field, wettability engineering is introduced as a strategy for the on-chip integration of electrolytes with micrometer-sized samples of 2D materials. Contact angles are systematically measured for a variety of electrolyte–surface couples to identify a rational device design, and engineer lateral contrasts in surface chemistry to control the rims of drop cast electrolytes with micrometer precision. This allows covering single crystalline flakes of 2D materials only partially, leaving most of the sample surface uncovered and imposing directionality on ion transport. Wettability engineering is used to fabricate few-layer graphene electrochemical micro two-compartment cells that display chemical diffusion of lithium on the order of 10^{-8} cm^2 s^{-1}. While the approach is transferrable to other 2D materials and ionic species, it can also benefit device design for the study of nonlocal electrolyte gating effects.

The properties of 2D layered materials regarding ion uptake, transfer, storage, and release receive increasing attention as differences from their bulk equivalents manifest.[1] Although layered materials consist of individual atomic layers, one or few of these layers taken alone are more than just the building block of the bulk. Instead, an entire field of interdisciplinary research today keeps being surprised about how much 2D materials are interesting in their own right. With the advent of graphene and 2D transition metal dichalcogenides, probably most of the excitement has been about the exotic electronic and optical properties of these materials.[2–6] Their controlled intercalation with ions is considered a powerful knob for tuning these properties.[7] Yet more understanding about the behavior of ions within 2D materials is needed. And although the extent to which the knowledge on bulk phases is applicable to the 2D case has still to be determined, it is already clear that van der Waals stacking of atomic layers with controllable twist opens possibilities to the study of ion insertion that have no bulk analog.[8,9]

To investigate 2D materials, a common route is to have them supported on the surface of a solid substrate. In this scenario, if ions are to be inserted on demand, i.e., via a control mechanism of some sort, they have to be put in contact with an electrolyte. The difference in chemical potential for a given species of ions in the 2D material with respect to a counter electrode provides a driving force for ion insertion that can be controlled. Although the substrate itself can serve as a solid-state electrolyte, as for example in the case of ion conducting glass ceramics,[10–12] ion insertion between the layers of a supported 2D material may be hampered due to the fact that efficient insertion typically proceeds via edges or defect sites. Covering these is more likely when applying an electrolyte from the top—an approach that has become widely used in recent years mostly for the sake of electrostatic gating.[13,14] For the purpose of addressing in a systematic manner ion insertion and transport, it is important to integrate electrolytes with 2D materials in a patterned way, such as for example to impose directionality on the ionic diffusion process. This is mainly a sample size and patterning resolution issue, which on the scale of 100 µm and beyond can be solved, e.g., by additive manufacturing of solid-state electrolytes[15] or by inkjet printing of liquid ones.[16–18] Current limitations of these approaches are set by printing resolution as well as by the mechanical properties of the electrolytes. As such, viscous electrolytes or ion-gels are more straight-forward to print,[16] while a range of low viscosity battery-grade electrolytes (such as $LiPF_6$ in ethylene carbonate/diethyl carbonate) are not. These tend to easily wet large portions of a sample's surface and must

---

Dr. M. Kühne[+], Dr. D. Zhao, Dr. U. Zschieschang,
Dr. H. Klauk, Dr. J. H. Smet
Max Planck Institute for Solid State Research
Stuttgart 70569, Germany
E-mail: j.smet@fkf.mpg.de

R. Buck, Dr. M. Müller
Fraunhofer Institute for Interfacial Engineering and Biotechnology
Stuttgart 70569, Germany

The ORCID identification number(s) for the author(s) of this article can be found under https://doi.org/10.1002/admi.202001453.

[+]Present address: Department of Chemical Engineering, Massachusetts Institute of Technology, Cambridge, MA 02139, USA

DOI: 10.1002/admi.202001453

thus be contained (also for reasons of non-negligible vapor pressure).[19,20] While future advances are expected to reduce achievable feature size in printing technology, the patterned integration of low-viscosity electrolytes on the micrometer scale likely demands alternative approaches.[21]

For feature sizes below 100 µm, lithographically patterned masks can be used that restrict the contact area of a much larger electrolyte with the sample under study. Such masks need to be ion-impenetrable dielectrics, a range of which have been successfully employed: Hard-baked photoresist,[22–24] SiO_2,[25,26] SU-8,[27,28] polymethyl methacrylate (PMMA),[29–34] alumina,[30] and hydrogen silsesquioxane (HSQ).[35] A potential disadvantage of this approach is that it typically entails also covering the rest of the sample with the mask material.

Here, we introduce wettability engineering as a mask-free alternative to achieving partial electrolyte coverage of a substrate-supported 2D material in a deterministic manner. The technique relies on drop-casting, which would easily cover a micron sized device fully,[36,37] onto a patterned surface that pins the advancing contact line of the spreading electrolyte to the border line with a region of higher contact angle. We report static contact angle values for three electrolytes used in the field after drop-casting: lithium perchlorate ($LiClO_4$) in poly(ethylene oxide) (PEO), LiTFSI in PEGMA/BEMA, and [DEME][TFSI] (see the Experimental Section for details). The latter serves as a proxy for [DEME][TFSI]-based binary salt mixtures such as [DEME][TFSI]-LiTFSI.[38,39] We present guiding principles for the integration of these electrolytes with micrometer-scale 2D material devices, the electrolyte-free parts of which remain entirely uncovered. In a next step we fabricate a wettability engineered micro two-compartment cell, inspired from the analysis of hydrogen permeation through solid metal, and use it to control and probe the room-temperature diffusion of Li in few-layer graphene. As opposed to a technique reported earlier,[40] here we do not require the application of very strong magnetic fields.

We first determine the static contact angles upon drop-casting of three electrolytes commonly used in the field: $LiClO_4$ in PEO (dissolved in acetonitrile), LiTFSI in PEGMA/BEMA, and [DEME][TFSI]. To this end, we deposit drops of each electrolyte solution on different surfaces and measure their static contact angle θ. In **Figure 1**a–d, we show results for LiTFSI in PEGMA/BEMA. This electrolyte wets Au better than SiO_2, as reflected by $\theta = 18°$ for Au and $\theta = 28.7°$ for SiO_2. To achieve larger values of θ, we prepare surfaces covered by self-assembled monolayers (SAMs) of molecules with nonpolar end groups. Figure 1c,d shows results obtained on octadecyltrichlorosilane (ODTS) and 12,12,13,13,14,14,15,15,16,16,17,17,18,18,18-pentadecylfluoro-octadecylphosphonic acid (FODPA) treated surfaces, respectively. The static contact angles, determined for all three electrolytes subject to this study, are shown in Figure 1e. As we present in the Supporting Information, we find the electrolyte surface tensions to be dominated by dispersive components that govern their interaction with substrate surfaces. More information on the different electrolytes and the surface preparation are given in the Experimental Section. In Figure 1e we also include static contact angles measured on commercial monolayer graphene (Graphenea, 300 nm SiO_2/Si substrates).

We exploit variations in wettability among surface terminations to fix position and course of an electrolyte drop's contact line. Using standard lithography tools, we create patterns on the surface of SiO_2-terminated Si substrates that a given electrolyte

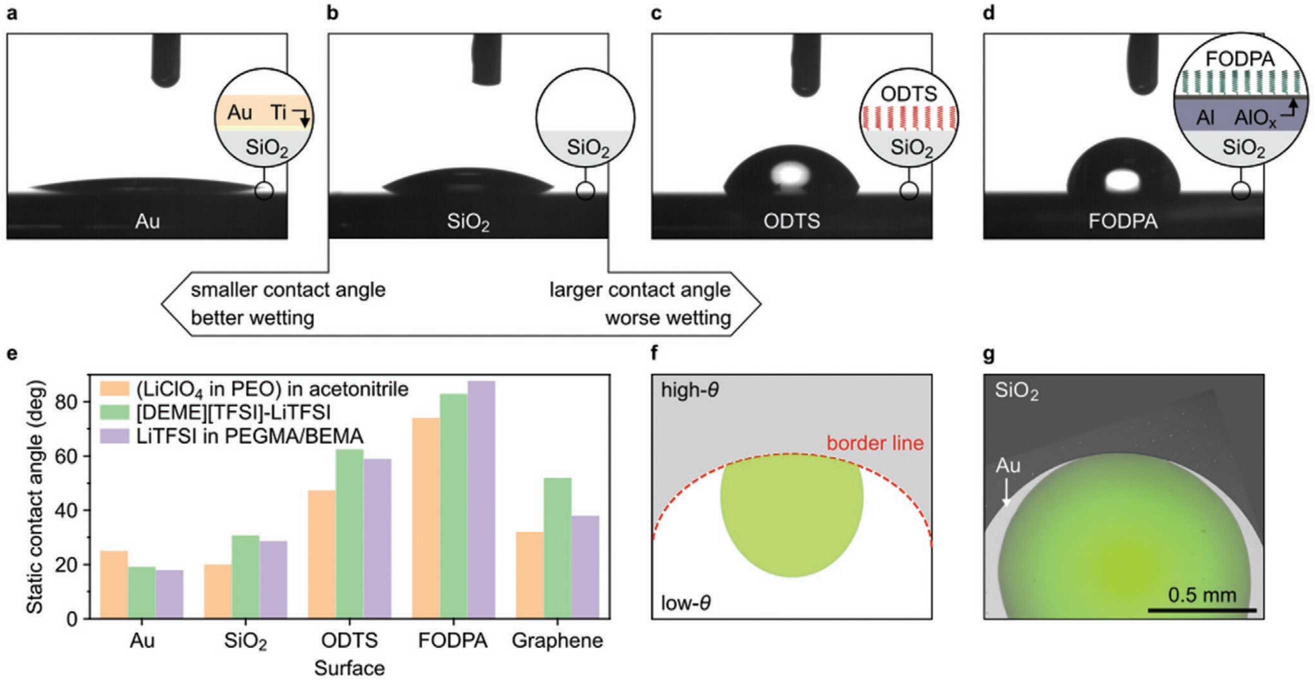

Figure 1. Electrolyte wetting. a–d) Static contact angle measurements of LiTFSI in PEGMA/BEMA electrolyte on different surfaces as indicated. e) Static contact angle of three electrolytes measured on different surfaces. f) Schematic top view of a drop cast electrolyte after spreading on a substrate with two patterned surface regions characterized by low and high contact angle θ. g) Optical micrograph of a LiTFSI in PEGMA/BEMA electrolyte after spreading on a substrate with wettability contrast as in (f).

wets either better or worse than SiO_2. The result is a surface exhibiting areal contrast in contact angle. The border line between regions of different wettability serves to pin the contact line of the electrolyte during drop-casting. Casting a drop onto a surface, its contact line advances until the drop shape reaches steady state. Ignoring contact angle hysteresis, this steady state is described by Young's equation.[41] However, on a low-θ region, spreading can be entirely stopped at the border to a high-θ region. This works well especially when the contrast in contact angle is large (imposing a high penalty on surface energy for wetting the high-θ region), the border line is smooth with a curvature close to the one of the equilibrium drop, and the encounter with the high-θ region happens near the end of spreading, i.e., when the velocity of the advancing contact line is small. The third point sets a constraint on the distance between the drop's center during drop-casting and the border to the high-θ region. Ideally, this distance is smaller than, yet comparable to, the radius R of the circular shape the drop assumes on an exclusively low-θ region. If chosen too small, the initial rapid spreading of the drop will entail wetting of the high-θ region which is undesirable in the context of this work. In Figure 1f we show the schematic equilibrium shape of an electrolyte after drop-casting onto a substrate with two surface regions differing in contact angle. As a desired result, the drop's contact line is partially pinned at the border to a high-θ region. Figure 1g is the optical micrograph of an electrolyte drop, here LiTFSI in PEGMA/BEMA, cast onto such a surface. Here, we chose Au as the low-θ region and SiO_2 as the high-θ region.

We now relax the condition of having a smooth border between low-θ and high-θ regions. Also, for the purpose of this work but with no loss of generality, we restrict the discussion to the border between SiO_2 and a region with either lower or higher contact angle θ. We design protrusions of SiO_2 into this region by patterning dents or gaps in its outline (**Figure 2**). After spreading, the contact line of the electrolyte drop still gets pinned at the remaining segments of the initial (not indented) border line. Moreover, the drop's contact line closely follows their projected continuation between segments. This holds as long as the separation between segments is about an order of magnitude smaller than the drop radius. For larger separations, deviations from the projected continuation become more noticeable. In the lower panel of Figure 2a we show the optical micrograph of a LiTFSI in PEGMA/BEMA drop after spreading. We find the drop's contact line to continue smoothly across narrow gaps in the pattern, but deviations occur from smooth continuation across larger gaps. For the given case of a drop with radius of ≈500 µm, the largest gap across which the course of the contact line remains visibly unaffected is 60 µm. From optical inspection, for gaps of this width or narrower, the contact line typically deviates by about +/− 1 µm or better from the projected continuation between adjacent border segments. This enables tailored on-chip integration of electrolyte drops with micrometer-sized samples. Depending on the pair of surface terminations chosen, different design strategies for taming the electrolyte drop can be envisaged, as we show in Figure 2.

In **Figure 3**a we present images of micro two-compartment cells fabricated using our wettability engineering strategy. As described in the Experimental Section, here we use mechanically exfoliated few-layer graphene transferred onto a SiO_2-terminated silicon substrate. The graphene flake is patterned using a combination of electron-beam lithography and O_2 plasma etching. We then created nonlithiating electrical contacts to the flake in a second electron-beam lithography step, followed by the deposition of 60 nm Ti. After a third lithography step, 60 nm Al is deposited, oxidized, and functionalized with

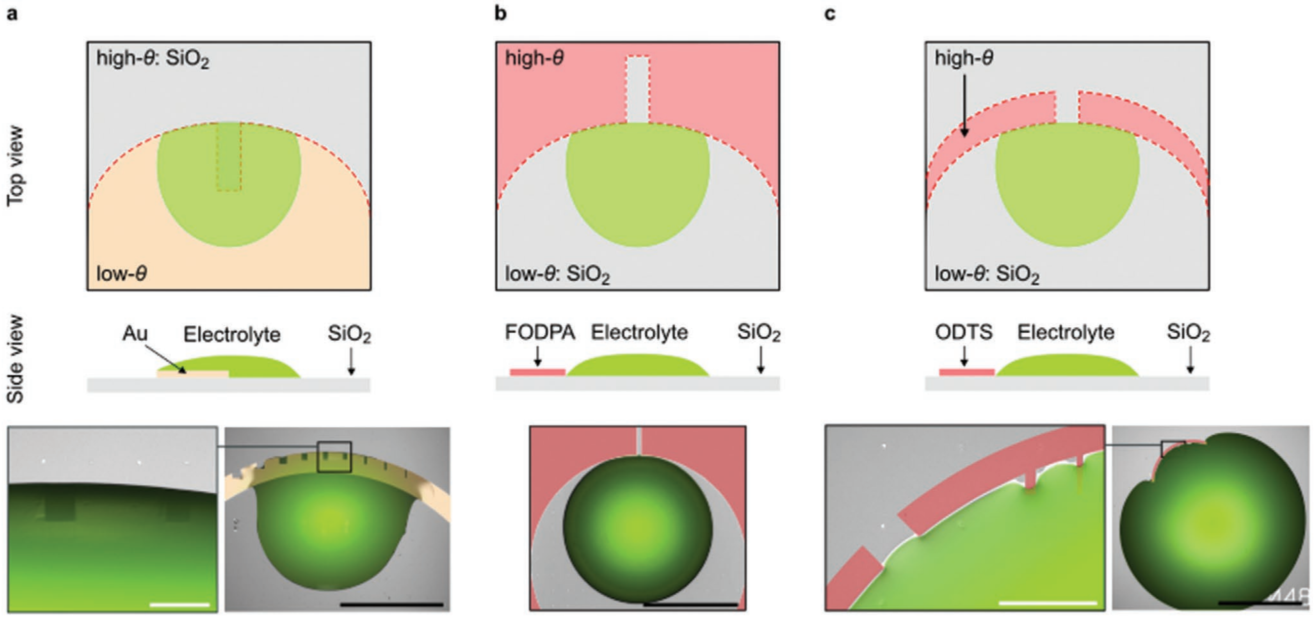

Figure 2. Wettability engineering. a–c) Schematic illustrations of different approaches used to determine position and course of a drop cast electrolyte's contact line after spreading (top and middle rows) as well as optical micrographs of realized samples (bottom row). White (black) scale bars are 100 µm (1 mm), respectively.

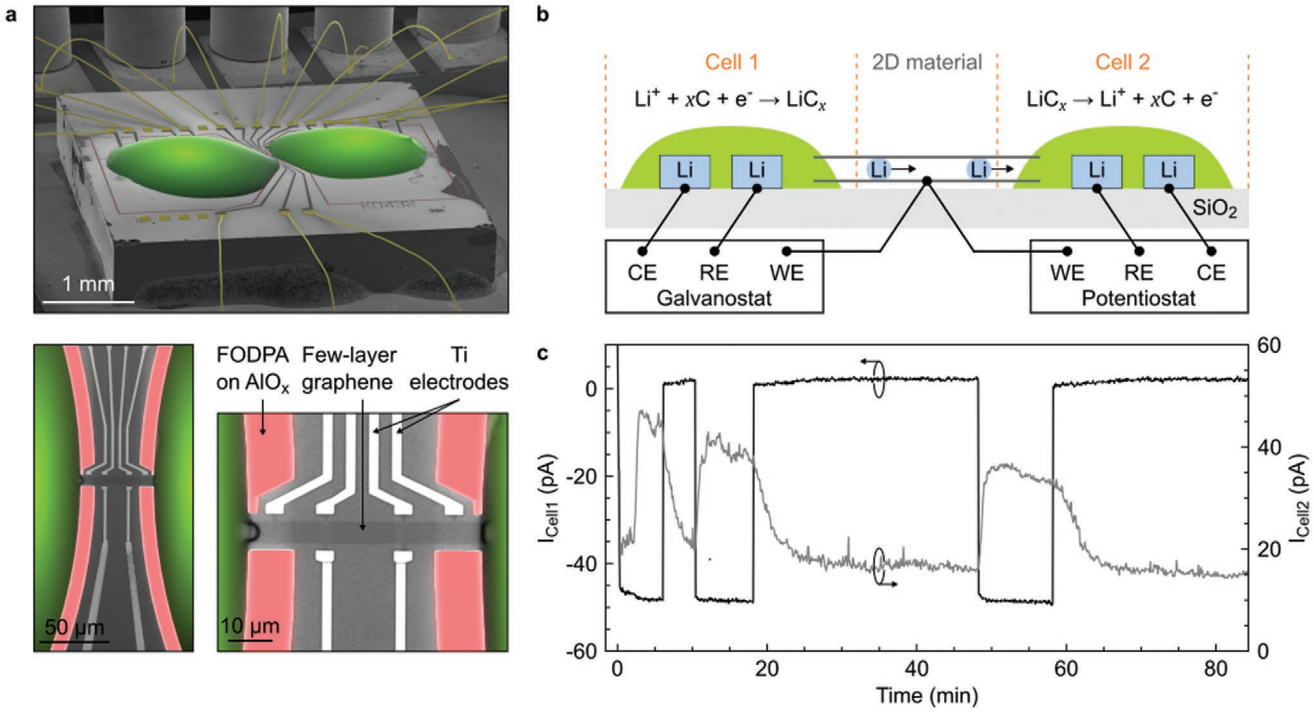

Figure 3. Wettability engineered micro two-compartment cells. a) Scanning-electron micrograph (top panel) and optical micrographs (bottom panels) of few-layer graphene devices with LiTFSI in PEGMA/BEMA electrolyte. The lower right is a zoom-in on the central region of the lower left micrograph. Red shading denotes high-θ regions modified with FODPA. b) Schematic of a two-compartment cell with a 2D material featuring as the common working electrode (WE). Li counter and reference electrodes are labeled as CE and RE, respectively. c) Measured chronoamperometric response I_{Cell2} of a few-layer graphene micro two-compartment cell to the intermittent galvanostatic polarization of the WE with I_{Cell1} in cell 1. In cell 2, the WE is potentiostatically polarized at 3 V versus Li/Li$^+$ throughout the course of the experiment.

FODPA to yield high-θ regions akin to the schematic shown in Figure 2c. As can be seen in the lower panel of Figure 3a, few layer graphene extends into designated openings of the FODPA barriers, resulting in only its two ends being covered by two LiTFSI in PEGMA/BEMA electrolyte drops. Small protrusions of electrolyte material onto the graphene, visible in the lower panel of Figure 3a, stem from device operation and were not observed on the as-fabricated device. Prior to electrolyte drop-casting, lithium metal was deposited onto designated Ti contact pads to realize the electrochemical two-compartment cell schematically shown in Figure 3b. Akin to the Devanathan–Stachurski cell,[42] initially designed for the investigation of hydrogen permeation through solid metal, the device comprises two electrochemical cells sharing a common working electrode (WE). Li metal serves as the counter electrodes CE$_1$ and CE$_2$ in cell 1 and 2, respectively. Persson et al. previously adapted the Devenathan–Stachurski scheme to study lithium diffusion.[43] Their implementation, however, required the use of macroscopic graphitic membranes.

In Figure 3c we show experimental data obtained from operating a few-layer graphene micro two-compartment cell using a bipotentiostat. In cell 1, the WE is repeatedly polarized galvanostatically at $I_{\mathrm{Cell1}} = -50$ pA, while in cell 2 we maintain the WE at a high anodic potential of 3 V versus Li/Li$^+$ throughout the course of the experiment. This leads to the immediate oxidation of Li having arrived in cell 2 from cell 1 via diffusion through the 2D material under study. The anodic current response in cell 2 thus reflects the deintercalative flux of ions from the WE and its time dependence bears information about ionic diffusivity. In Figure 3c, we plot the chronoamperometric response of cell 2 that results from the repeated application of a 50 pA current in cell 1. The device shows limited cycling stability likely related to a parasitic effect responsible for offsetting the anodic current from zero by ≈15 pA. Also, the reduced Coulombic efficiency of the redox processes in cells 1 and 2, here at most on the order of 60%, may indicate non-negligible side reactions. As can be seen, galvanostatic polarization in cell 1 results in a steep increase of the anodic current measured in cell 2 until it reaches a plateau. Upon removing the galvanostatic polarization in cell 1, the anodic current in cell 2 decreases and converges toward its initial value. Given the approximately linear configuration of the device, we can model lithium diffusion according to Fick's second law

$$\frac{\partial c_{\mathrm{Li}}}{\partial t} = D^{\delta}\frac{\partial^2 c_{\mathrm{Li}}}{\partial x^2} \tag{1}$$

where c_{Li} is the lithium concentration at time t and position x, and D^{δ} is the chemical diffusion coefficient of lithium. We solve Equation (1) with a standard differential equation solver, given the initial condition

$$c_{\mathrm{Li}}(x, t = 0) = 0 \tag{2}$$

and the boundary conditions

$$c_{\mathrm{Li}}(x=0, t>0) = c_0, \text{and } c_{\mathrm{Li}}(x=L, t>0) = 0 \tag{3}$$

Here, the electrolyte-uncovered region of the few-layer graphene WE starts at $x = 0$ and ends at $x = L$. As in ref. [43], we consider galvanostatic polarization to cause a constant concentration c_0 of Li at the WE/electrolyte interface in cell 1. The ionic flux j into cell 2 is given by Fick's first law as

$$j = -D^{\delta} \left.\frac{\partial c_{\mathrm{Li}}}{\partial x}\right|_{x=L} \tag{4}$$

and can be related to the current according to Faraday's law of electrolysis

$$I_{\mathrm{Cell2}}(t) = -n_{\mathrm{e}} FAj = FAD^{\delta} \left.\frac{\partial c_{\mathrm{Li}}}{\partial x}\right|_{x=L} \tag{5}$$

Here, $n_{\mathrm{e}} = 1$ is the number of electrons involved in the relevant electrochemical reaction (Figure 3b), F is the Faraday constant, and $A = 5\ \mu\mathrm{m} \cdot (n-1) \cdot 0.335\ \mathrm{nm}$ is the cross-sectional area of the 5 µm wide working electrode consisting of n graphene layers with interlayer distance 0.335 nm. Since here both c_0 and D^{δ} are fit parameters, we do not need to rely on knowing the exact layer number n, since $A \cdot c_0$ only affects the amplitude of the anodic current response while D^{δ} determines its time dependence (in fact we use "$A \cdot c_0$" as a fit parameter). This can be seen directly in the expression of Equation (5) that we obtain by solving Equation (1)

$$I_{\mathrm{Cell2}}(t) = FD^{\delta} \frac{A \cdot c_0}{L} \left[1 + 2\sum_{k=1}^{\infty} \exp\left(-\frac{D^{\delta}\pi^2 k^2 t}{L^2}\right) \cos(\pi k)\right] \tag{6}$$

The term in the square bracket is a theta function.

We use Equation (6) to fit the anodic current response measured in cell 2 separately for each of the three galvanostatic polarization cycles (**Figure 4**). Best fits to the data are obtained by standard nonlinear least squares fitting with values of D^{δ} as stated in the figure. As mentioned above, we allow for a constant offset in current for each dataset. Except for the first galvanostatic polarization cycle, we find that the anodic current response measured in cell 2 is well described by the model. Overall the values determined for D^{δ} appear low compared with in-plane lithium diffusion in graphitic carbon.[43] Also, D^{δ} was previously shown to attain about three orders of magnitudes larger values in bilayer graphene.[40] However, in contrast to this work, in ref. [40] the lithium concentration was measured simultaneously at several locations along an elongated graphene bilayer, allowing to extract the in-plane diffusion kinetics more directly. If we think of the approach in ref. [40] as a four-point probe experiment, the one here would be a two-point analog. Thus, although we find our model to show good agreement with the data in Figure 4, the low Faradaic efficiency points to non-negligible side-reactions. These are likely associated with a resistive solid electrolyte interphase (SEI) growing at the lithium electrodes, due to the poor stability of LiTFSI in PEGMA/BEMA with lithium metal demonstrated previously.[40] Impedance measurements to subtract this SEI contribution would allow for a more accurate estimation of the lithium chemical diffusion coefficient, as is customary in the characterization of liquid electrolytes.[44,45] A practical approach targeting to minimize this undesirable effect would consist in replacing lithium metal with a less reactive electrode material, such as $\mathrm{LiC_6}$.

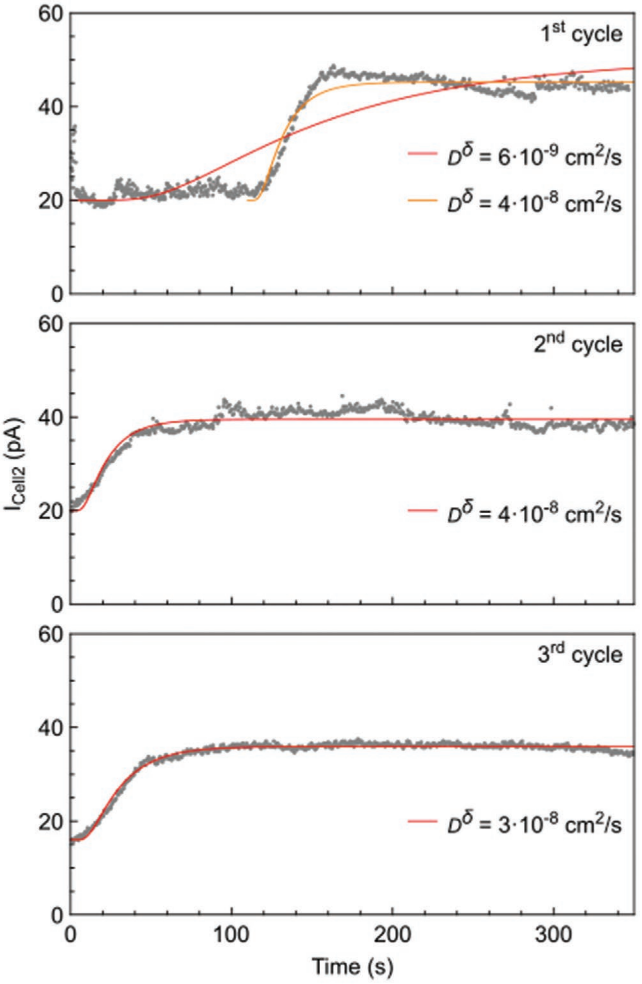

Figure 4. Measured chronoamperometric response I_{Cell2} of a few-layer graphene micro two-compartment cell to the intermittent galvanostatic polarization I_{Cell1} of cell 1 (gray, data as in Figure 3d). Red and orange lines are least-square fits obtained with the indicated values for the lithium chemical diffusion coefficient D^{δ}.

We qualify wettability engineering as an approach to integrate electrolytes in 2D material devices in a deterministic manner. Using this method, we fabricate the first on-chip electrochemical micro two-compartment cell with a single-crystalline few-layer graphene flake serving as shared working electrode. We demonstrate controlled lithium insertion and directed diffusion, here characterized by a comparatively low chemical diffusion coefficient yet to be optimized. The proposed strategy complements existing approaches to tailored integration of electrolytes in on-chip device applications, and in principle may be scaled through the use of microsyringes, microprinters, or dip pen nanolithography for controlled and automated electrolyte deposition. We believe it will contribute to further advances in the field of iontronics and the study of intercalation-induced effects in 2D materials systems.

Experimental Section

Electrolytes: "$LiClO_4$ in PEO" denotes $LiClO_4$ dissolved in PEO, average molecular weight M = 100 000 g mol^{-1}. This electrolyte was prepared by dissolving a ≈1:1.27 w/w mixture of $LiClO_4$ and PEO in anhydrous acetonitrile (CH_3CN) at a concentration of 100 mg mL^{-1}, yielding an ether-oxygen-to-lithium ratio (EO/Li) of 4:1. The solution was stirred over night at 50 °C and then passed through a 0.2 µm poly(tetrafluoroethylene) (PTFE) filter. The density of the solution is $\rho_{\mathrm{LiClO_4,inPEO}} \approx 1.13\ \mathrm{gcm^{-3}}$. More information on this electrolyte can be found in ref. [46] and references therein.

"LiTFSI in PEGMA/BEMA" denotes 0.35 M lithium bis (trifluoromethane) sulfonimide (LiTFSI) in polyethylene glycol methyl ether methacrylate:bisphenol A ethoxylate dimethacrylate (PEGMA:BEMA) w/w 3:7 with an added 2–4 wt% of 2-hydroxy-2-methylpropiophenone, a common photoinitiator. The density of the electrolyte is $\rho_{\mathrm{LiTFSI\ in\ PEGMA/BEMA}} \approx 0.84\ \mathrm{g\,cm^{-3}}$. More information on this electrolyte can be found in.[40,47]

"[DEME][TFSI]" denotes *N*,*N*-diethyl-*N*-methyl-*N*-(2-methoxyethyl) ammonium bis (tri-fluoromethane) sulfonimide. The density of this ionic liquid is $\rho_{\mathrm{DEME\text{-}TFSI}} \approx 1.38\ \mathrm{g\ cm^{-3}}$. This ionic liquid was widely used in the field in its pure form for electrolyte gating purposes, but also binary salt mixtures with LiTFSI have been explored for Li–O_2 batteries.[39] No difference was observed in static contact angle after drop-casting this electrolyte on commercial monolayer graphene (Graphenea, 300 nm SiO_2/Si substrates), both with and without a small addition of LiTFSI (10 wt%).

Contact Angle Measurements: Static contact angles of electrolytes were determined at room temperature by the sessile drop method using a contact angle goniometer (Erma G-1). To prevent gravitational distortion, drops of ≈2 µL volume were cast onto solid surfaces using a microsyringe. The static contact angle was measured immediately after spreading and on multiple samples. The images of 2 µL drops in Figure 1a–d were taken with a video contact angle measurement system (OCA40, Dataphysics Instruments, 48% relative humidity).

Wettability Engineering: Square pieces cut from 300 nm SiO_2-terminated Si-wafers served as substrates for the on-chip devices.

Au: A fresh gold (Au) surface was created by physical vapor deposition of 5 nm Ti (as an adhesion layer) followed by 25 nm Au.

ODTS: A self-assembled monolayer (SAM) of octadecyltrichlorosilane (CH3(CH2)17SiCl3, ODTS) was formed on SiO_2. To this end the substrate was first exposed to oxygen plasma. The substrate as well as a few drops of ODTS were then placed inside an oven and kept at a temperature of 170 °C for a few hours. During this process, the ODTS molecules from the vapor phase formed a smooth, densly packed monolayer by bonding covalently to OH groups on the SiO_2 surface under the formation of HCl gas. See ref. [48] for more information on this type of SAM.

FODPA: A SAM of 12,12,13,13,14,14,15,15,16,16,17,17,18,18,18-pentadecylfluoro-octadecylphosphonic acid ($C_7F_{15}C_{11}H_{22}PO(OH)_2$, FODPA) was formed on AlO_x. To this end Al, previously evaporated onto a target substrate, was exposed to oxygen plasma, thereby forming an AlO_x surface with unsaturated OH groups. The substrate was then immersed into a 2-propanol solution of FODPA, allowing a monolayer to self-assemble on the AlO_x. See ref. [49] for more information on this type of SAM.

Device Fabrication: Graphene flakes were obtained by mechanical exfoliation from bulk graphite (NGS Naturgraphit GmbH) using adhesive tape onto a sacrificial PMMA layer. Large flakes with typically at least one lateral dimension exceeding 50 µm were selected based on the optical contrast. A dry transfer technique was deployed to position the flake on the target SiO_2-terminated silicon substrate.[50] Electron beam lithography was used to pattern PMMA masks for shaping and/or isolating the flakes of interest via O_2-plasma etching, as well as for the lift-off of metallic contacts to the bilayer flake and the counter-electrode contact for the electrochemical cell. The deposition of lithium as well as the electrolyte was done in an Ar-filled glovebox. Microliter drops of LiTFSI in PEGMA/BEMA electrolyte were placed using a microstreaker and subsequently solidified by ultraviolet curing.

Supporting Information

Supporting Information is available from the Wiley Online Library or from the author.

Acknowledgements

The Baden-Württemberg Stiftung as well as the EU graphene flagship core 3 and the DFG graphene priority program (SPP 1459) are acknowledged. Matthias Schlörholz is acknowledged for the synthesized FODPA. Klaus von Klitzing is thanked for discussions and support. Doris Vollmer and Maria d'Acunzi are thanked for fruitful discussions. Federico Paolucci is thanked for discussions at an early stage of this work, and Jelena Popovic is thanked for input on the manuscript.

Open access funding enabled and organized by Projekt DEAL.

Conflict of Interest

The authors declare no conflict of interest.

Keywords

2D materials, electrolyte, ion diffusion, ion transport, wettability

Received: August 18, 2020
Revised: October 29, 2020

---

[1] M. S. Stark, K. L. Kuntz, S. J. Martens, S. C. Warren, *Adv. Mater.* **2019**, *31*, 1808213.

[2] Q. H. Wang, K. Kalantar-Zadeh, A. Kis, J. N. Coleman, M. S. Strano, *Nat. Nanotechnol.* **2012**, *7*, 699.

[3] G. Fiori, F. Bonaccorso, G. Iannaccone, T. Palacios, D. Neumaier, A. Seabaugh, S. K. Banerjee, L. Colombo, *Nat. Nanotechnol.* **2014**, *9*, 768.

[4] X. Li, L. Tao, Z. Chen, H. Fang, X. Li, X. Wang, J. Bin Xu, H. Zhu, *Appl. Phys. Rev.* **2017**, *4*, 021306.

[5] S. Bertolazzi, P. Bondavalli, S. Roche, T. San, S. Y. Choi, L. Colombo, F. Bonaccorso, P. Samorì, *Adv. Mater.* **2019**, *31*, 1806663.

[6] L. Kong, Y. Chen, Y. Liu, *Nano Res.* **2020**, https://doi.org/10.1007/s12274-020-2958-7.

[7] J. Wan, S. D. Lacey, J. Dai, W. Bao, M. S. Fuhrer, L. Hu, *Chem. Soc. Rev.* **2016**, *45*, 6742.

[8] S. Y. F. Zhao, G. A. Elbaz, D. K. Bediako, C. Yu, D. K. Efetov, Y. Guo, J. Ravichandran, K.-A. Min, S. Hong, T. Taniguchi, K. Watanabe, L. E. Brus, X. Roy, P. Kim, *Nano Lett.* **2018**, *18*, 460.

[9] D. K. Bediako, M. Rezaee, H. Yoo, D. T. Larson, S. Y. F. Zhao, T. Taniguchi, K. Watanabe, T. L. Brower-Thomas, E. Kaxiras, P. Kim, *Nature* **2018**, *558*, 425.

[10] B. Lei, N. Z. Wang, C. Shang, F. B. Meng, L. K. Ma, X. G. Luo, T. Wu, Z. Sun, Y. Wang, Z. Jiang, B. H. Mao, Z. Liu, Y. J. Yu, Y. B. Zhang, X. H. Chen, *Phys. Rev. B* **2017**, *95*, 020503.

[11] M. Philippi, I. Gutiérrez-Lezama, N. Ubrig, A. F. Morpurgo, *Appl. Phys. Lett.* **2018**, *113*, 033502.

[12] M. Liao, Y. Zhu, J. Zhang, R. Zhong, J. Schneeloch, G. Gu, K. Jiang, D. Zhang, X. Ma, Q. K. Xue, *Nano Lett.* **2018**, *18*, 5660.

[13] S. H. Kim, K. Hong, W. Xie, K. H. Lee, S. Zhang, T. P. Lodge, C. D. Frisbie, *Adv. Mater.* **2013**, *25*, 1822.

[14] S. Z. Bisri, S. Shimizu, M. Nakano, Y. Iwasa, *Adv. Mater.* **2017**, *29*, 1607054.

[15] D. W. McOwen, S. Xu, Y. Gong, Y. Wen, G. L. Godbey, J. E. Gritton, T. R. Hamann, J. Dai, G. T. Hitz, L. Hu, E. D. Wachsman, *Adv. Mater.* **2018**, *30*, 1707132.

[16] J. H. Cho, J. Lee, Y. Xia, B. Kim, Y. He, M. J. Renn, T. P. Lodge, C. Daniel Frisbie, *Nat. Mater.* **2008**, *7*, 900.

[17] S. Dasgupta, R. Kruk, N. Mechau, H. Hahn, *ACS Nano* **2011**, *5*, 9628.

[18] S. H. Kim, K. Hong, K. H. Lee, C. D. Frisbie, *ACS Appl. Mater. Interfaces* **2013**, *5*, 6580.

[19] W. Bao, J. Wan, X. Han, X. Cai, H. Zhu, D. Kim, D. Ma, Y. Xu, J. N. Munday, H. D. Drew, M. S. Fuhrer, L. Hu, *Nat. Commun.* **2014**, *5*, 4224.

[20] F. Xiong, H. Wang, X. Liu, J. Sun, M. Brongersma, E. Pop, Y. Cui, *Nano Lett.* **2015**, *15*, 6777.

[21] B. Prasad, G. Pfanzelt, E. Fillis-Tsirakis, M. J. Zachman, L. F. Kourkoutis, J. Mannhart, *Adv. Mater.* **2018**, *30*, 1802598.

[22] K. Ueno, S. Nakamura, H. Shimotani, A. Ohtomo, N. Kimura, T. Nojima, H. Aoki, Y. Iwasa, M. Kawasaki, *Nat. Mater.* **2008**, *7*, 855.

[23] M. Lee, J. R. Williams, S. Zhang, C. D. Frisbie, D. Goldhaber-Gordon, *Phys. Rev. Lett.* **2011**, *107*, 256601.

[24] E. Uesugi, H. Goto, R. Eguchi, A. Fujiwara, Y. Kubozono, *Sci. Rep.* **2013**, *3*, 1595.

[25] J. T. Ye, S. Inoue, K. Kobayashi, Y. Kasahara, H. T. Yuan, H. Shimotani, Y. Iwasa, *Nat. Mater.* **2010**, *9*, 125.

[26] J. T. Ye, Y. J. Zhang, R. Akashi, M. S. Bahramy, R. Arita, Y. Iwasa, *Science* **2012**, *338*, 1193.

[27] L. H. Hess, M. V. Hauf, M. Seifert, F. Speck, T. Seyller, M. Stutzmann, I. D. Sharp, J. A. Garrido, *Appl. Phys. Lett.* **2011**, *99*, 033503.

[28] G. Froehlicher, S. Berciaud, *Phys. Rev. B* **2015**, *91*, 205413.

[29] Y. Yu, F. Yang, X. F. Lu, Y. J. Yan, Y. Cho, L. Ma, X. Niu, S. Kim, Y. Son, D. Feng, S. Li, S. Cheong, X. H. Chen, Y. Zhang, *Nat. Nanotechnol.* **2015**, *10*, 270.

[30] P. Gallagher, M. Lee, T. A. Petach, S. W. Stanwyck, J. R. Williams, K. Watanabe, T. Taniguchi, D. Goldhaber-Gordon, *Nat. Commun.* **2015**, *6*, 6437.

[31] C. Peng, S. Nanot, R.-J. Shiue, G. Grosso, Y. Yang, M. Hempel, P. Jarillo-Herrero, J. Kong, F. H. L. Koppens, D. K. Efetov, D. Englund, *New J. Phys.* **2018**, *20*, 083050.

[32] Y. Nakagawa, Y. Saito, T. Nojima, K. Inumaru, S. Yamanaka, Y. Kasahara, Y. Iwasa, *Phys. Rev. B* **2018**, *98*, 064512.

[33] Y. He, Q. He, L. Wang, C. Zhu, P. Golani, A. D. Handoko, X. Yu, C. Gao, M. Ding, X. Wang, F. Liu, Q. Zeng, P. Yu, S. Guo, B. I. Yakobson, L. Wang, Z. W. Seh, Z. Zhang, M. Wu, Q. J. Wang, H. Zhang, Z. Liu, *Nat. Mater.* **2019**, *18*, 1098.

[34] B. Wu, X. Wang, H. Tang, W. Jiang, Y. Chen, Z. Wang, Z. Cui, T. Lin, H. Shen, W. Hu, X. Meng, W. Bao, J. Wang, J. Chu, *Small* **2020**, *16*, 2000420.

[35] S. Grover, A. Joshi, A. Tulapurkar, M. M. Deshmukh, *Sci. Rep.* **2017**, *7*, 3336.

[36] A. Das, S. Pisana, B. Chakraborty, S. Piscanec, S. K. Saha, U. V. Waghmare, K. S. Novoselov, H. R. Krishnamurthy, A. K. Geim, A. C. Ferrari, A. K. Sood, *Nat. Nanotechnol.* **2008**, *3*, 210.

[37] B. Wu, X. Wang, H. Tang, T. Lin, H. Shen, W. Hu, X. Meng, W. Bao, J. Wang, J. Chu, *Sci. China Inf. Sci.* **2019**, *62*, 220405.

[38] S. Drvarič Talian, M. Bešter-Rogač, R. Dominko, *Electrochim. Acta* **2017**, *252*, 147.

[39] U. Ulissi, G. A. Elia, S. Jeong, F. Mueller, J. Reiter, N. Tsiouvaras, Y. K. Sun, B. Scrosati, S. Passerini, J. Hassoun, *ChemSusChem* **2018**, *11*, 229.

[40] M. Kühne, F. Paolucci, J. Popovic, P. M. Ostrovsky, J. Maier, J. H. Smet, *Nat. Nanotechnol.* **2017**, *12*, 895.

[41] D. Bonn, J. Eggers, J. Indekeu, J. Meunier, *Rev. Mod. Phys.* **2009**, *81*, 739.

[42] M. A. V. Devanathan, Z. Stachurski, *Proc. R. Soc. A* **1962**, *270*, 90.

[43] K. Persson, V. A. Sethuraman, L. J. Hardwick, Y. Hinuma, Y. S. Meng, A. van der Ven, V. Srinivasan, R. Kostecki, G. Ceder, *J. Phys. Chem. Lett.* **2010**, *1*, 1176.

[44] J. Popovic, G. Hasegawa, I. Moudrakovski, J. Maier, *J. Mater. Chem. A* **2016**, *4*, 7135.

[45] M. Nojabaee, J. Popovic, J. Maier, *J. Mater. Chem. A* **2019**, *7*, 13331.

[46] S. K. Fullerton-Shirey, J. K. Maranas, *Macromolecules* **2009**, *42*, 2142.

[47] J. R. Nair, C. Gerbaldi, M. Destro, R. Bongiovanni, N. Penazzi, *React. Funct. Polym.* **2011**, *71*, 409.

[48] D. K. Aswal, S. Lenfant, D. Guerin, J. V. Yakhmi, D. Vuillaume, *Anal. Chim. Acta* **2006**, *568*, 84.

[49] R. Luschtinetz, A. F. Oliveira, J. Frenzel, J.-O. Joswig, G. Seifert, H. A. Duarte, *Surf. Sci.* **2008**, *602*, 1347.

[50] C. R. Dean, A. F. Young, I. Meric, C. Lee, L. Wang, S. Sorgenfrei, K. Watanabe, T. Taniguchi, P. Kim, K. L. Shepard, J. Hone, *Nat. Nanotechnol.* **2010**, *5*, 722.

Supporting Information

Wettability Engineering for Studying Ion Transport in 2D Layered Materials

*Matthias Kühne, Dong Zhao, Ute Zschieschang, Regina Buck, Michaela Müller, Hagen Klauk, and Jurgen H. Smet**

Fowkes[S1] suggested that the surface tension γ_i of a liquid i (respectively the surface free energy of a solid) can be written as the sum of contributions j from different classes of interactions, i.e.,

$$\gamma_i = \sum_i \gamma_i^j. \tag{S1}$$

The most important classes of interactions have however been identified in different ways. Here, we consider the approaches of Owens, Wendt, Rabel, and Kaelble (OWRK),[S2–S4] as well as van Oss, Chaudhury, and Good (vOCG).[S5]

In the OWRK framework, the most important components of the surface tension γ_i of material i are γ_i^{D} and γ_i^{P}, stemming from dispersive (D) and polar (P) interactions, respectively. Equation S1 can thus be stated as

$$\gamma_i = \gamma_i^{\mathrm{D}} + \gamma_i^{\mathrm{P}}.$$

Measuring the contact angle of a set of suited reference liquids on a solid surface, γ_s can be determined using the modified Young equation

$$\gamma_l(1 + \cos\theta) = 2\sqrt{\gamma_l^{\mathrm{D}}\gamma_s^{\mathrm{D}}} + 2\sqrt{\gamma_l^{\mathrm{P}}\gamma_s^{\mathrm{P}}}. \tag{S2}$$

We use the set of five liquids with tabulated surface tension parameters as given in Table S1. Using this set, we determine the surface tension values γ_s for seven surfaces using a least square fit to Equation S2. We obtain the values stated in Table S2.

Table S1. Surface tension parameters of liquids at room temperature in mJ/m^2 according to [S6].

	γ_l	γ_l^{D}	γ_l^{P}	γ_l^{LW}	γ_l^{+}	γ_l^{-}	γ_l^{AB}
H_2O	72.8	21.8	51	21.8	25.5	25.5	51
n-Hexadecane	27.47	27.47	0	27.47	0	0	0
Glycerol	64	34	30	34	3.92	57.4	30
Dimethylsulfoxide	44	36	8	36	0.5	32	8
Diiodomethane	50.8	50.8	0	50.8	0	0	0

Table S2. Surface free energy values of solids at room temperature in mJ/m^2, calculated from measured contact angle data.

	OWRK			vOCG				
	γ_s^{D}	γ_s^{P}	γ_s	γ_s^{LW}	γ_s^{+}	γ_s^{-}	γ_s^{AB}	γ_s
Au	33.76	7.44	41.2	34.82	0.15	19.63	3.42	38.23
SiO_2	30.13	10.79	40.92	29.97	1.88	11.01	9.11	39.08
SiO_2 (O_2 plasma)	29.22	33.9	63.12	30.82	1.76	66.19	21.56	52.38
ODTS	27.32	0.18	27.5	27.39	0.01	0.42	0.12	27.51
ODPA	24.73	0.03	24.76	24.8	0	0.13	0	24.8
FODPA	11.52	0	11.52	11.44	0	0.02	0	11.44
Polystyrol	32.23	2.92	35.15	32.92	0.05	7.83	1.25	34.17

In the vOCG framework, the most important components of the surface tension γ_i of material i are γ_i^{LW} and γ_i^{AB}, stemming from Lifshitz-van der Waals (LW) and Lewis acid-base (AB) interactions, respectively. Equation S1 can thus be stated as

$$\gamma_i = \gamma_i^{\mathrm{LW}} + \gamma_i^{\mathrm{AB}}.$$

The polar component γ_i^{AB} can further be written as

$$\gamma_i^{\mathrm{AB}} = 2\sqrt{\gamma_i^{+}\gamma_i^{-}},$$

where γ_i^{+} is the electron acceptor parameter and γ_i^{-} is the electron donor parameter. The Young equation to consider acquires the form

$$\gamma_l(1+\cos\theta) = 2\sqrt{\gamma_l^{\mathrm{LW}}\gamma_s^{\mathrm{LW}}} + 2\sqrt{\gamma_l^{+}\gamma_s^{-}} + 2\sqrt{\gamma_l^{-}\gamma_s^{+}}. \tag{S3}$$

Again using the set of five liquids with tabulated surface tension parameters as given in Table S1, we determine the surface tension values γ_s for seven surfaces using a least square fit to Equation S3. We obtain the values stated in Table S2. An alternative two-step approach consisting in fitting data from non-polar liquids first using the reduced equation

$$1 + \cos\theta = 2\sqrt{\frac{\gamma_s^{\mathrm{LW}}}{\gamma_l^{\mathrm{LW}}}}$$

to determine γ_s^{LW}, followed by fitting data from polar liquids using Equation S3, resulted in $< 1\ \%$ variation in values of the best fit parameters only.

In order to determine the surface tension components of our three electrolytes, we measure their contact angles on the set of seven different surfaces given in Table S2. Results are summarized in Table S3. The absolute liquid surface tension values γ_l of our electrolytes were determined from drop shape analysis, see Table S4. By fitting the overdetermined set of contact angle data by Equations S2 or S3, respectively, we obtain all other values given in Table S4.

Table S3. Static contact angles (in units of deg) of electrolytes measured on the surface of different solids. These measurements were taken partially using a video contact angle measurement system (DataPhysics) and partially by eye using an analog contact angle measurement setup. We state mean values of 2 or more repeated measurements and include uncertainties in last digits (standard deviations) if readings differed.

	LiTFSI in PEGMA/BEMA	$LiClO_4$ in PEO	[DEME][TFSI]
Au	18	25	19.1(17)
SiO_2	28.7(9)	20	30.8(5)
SiO_2 (O_2 plasma)	12	10	19
ODTS	59	47.3(25)	62.5(15)
ODPA	68	58.7(9)	69.5(15)
FODPA	87.7(5)	74(3)	82.9(9)
Polystyrol	20(1)	27(1)	20

Table S4. Surface tension values of electrolytes at room temperature in mJ/m^2. γ_l values were obtained from three repeated drop shape analyses (DataPhysics).

	γ_l	γ_l^{D}	γ_l^{P}	γ_l^{LW}	γ_l^{+}	γ_l^{-}	γ_l^{AB}
LiTFSI in PEGMA/BEMA	40.10(4)	38.70	1.40	37.86	0.24	5.22	2.24
$LiClO_4$ in PEO	29.36(1)	29.36	0	17.87	1.10	29.91	11.49
[DEME][TFSI]	33.71(2)	33.71	0	22.65	1.13	27.11	11.06

References

[S1] F. M. Fowkes, *J. Phys. Chem.* **1962**, *66*, 382.

[S2] D. K. Owens, R. C. Wendt, *J. Appl. Polym. Sci.* **1969**, *13*, 1741.

[S3] D. H. Kaelble, *J. Adhes.* **1970**, *2*, 66.

[S4] W. Rabel, *Farbe und Lack* **1971**, *77*, 997.

[S5] C. J. van Oss, M. K. Chaudhury, R. J. Good, *Chem. Rev.* **1988**, *88*, 927.

[S6] F. M. Etzler, in *Contact Angle, Wettability and Adhesion Vol. 3* (Ed: K. L. Mittal), VSP, Utrecht-Boston, **2003**, pp. 219–264.